

Article

A Systematic Method for Designing a PR Controller and Active Damping of the LCL Filter for Single-Phase Grid-Connected PV Inverters

Ningyun Zhang *, Houjun Tang and Chen Yao

School of Electronic Information and Electrical Engineering, Shanghai Jiao Tong University, 800 Dongchuan Rd, Minhang District, Shanghai 200240, China;

E-Mails: hjtang@sjtu.edu.cn (H.T.); chen1834@sjtu.edu.cn (C.Y.)

* Author to whom correspondence should be addressed; E-Mail: zhangningyun11@sjtu.edu.cn; Tel.: +86-21-3420-4604.

Received: 3 March 2014; in revised form: 13 June 2014 / Accepted: 17 June 2014 /

Published: 24 June 2014

Abstract: The Proportional Resonant (PR) current controller provides gains at a certain frequency (resonant frequency) and eliminates steady state errors. Therefore, the PR controller can be successfully applied to single grid-connected PV inverter current control. On the contrary, a PI controller has steady-state errors and limited disturbance rejection capability. Compared with the L- and LC filters, the LCL filter has excellent harmonic suppression capability, but the inherent resonant peak of the LCL filter may introduce instability in the whole system. Therefore, damping must be introduced to improve the control of the system. Considering the controller and the LCL filter active damping as a whole system makes the controller design method more complex. In fact, their frequency responses may affect each other. The traditional trial-and-error procedure is too time-consuming and the design process is inefficient. This paper provides a detailed analysis of the frequency response influence between the PR controller and the LCL filter regarded as a whole system. In addition, the paper presents a systematic method for designing controller parameters and the capacitor current feedback coefficient factor of LCL filter active-damping. The new method relies on meeting the stable margins of the system. Moreover, the paper also clarifies the impact of the grid on the inverter output current. Numerical simulation and a 3 kW laboratory setup assessed the feasibility and effectiveness of the proposed method.

Keywords: single phase; grid-connected; LCL filter; active damping; proportional resonant (PR) controller

1. Introduction

The rapid increase in global energy consumption has accelerated the need for greener energy sources. Nowadays, renewable, highly sustainable energies derived from inexhaustible sources such as wind, photovoltaic, or tides have attracted much more attention [1]. Distributed power generation systems (DPGS) are attractive both for the market and for researchers, and the most important part of a DPGS, the grid-connected inverter, is a research hotspot.

The filter is an essential component that suppresses the harmonics introduced through the Pulse-Width Modulation (PWM) technique used in grid-connected inverters. Thanks to the excellent harmonic suppression ability an LCL filter topology is much more attractive than L and LC filters. However, the LCL filter generates significant resonance peaks that worsen the system stability, and the control scheme design of grid-connected inverters take into consideration this behavior. Damping the filter resonance overcomes LCL filter oscillations and stabilizes the system [2,3]. Simple passive damping with a resistor connected in series or parallel to the LCL filter capacitor, results in additional power loss and decreases the LCL filter performance [4]. Papers in the literature present different active damping methods. The so-called ‘active damping by well-designed control algorithm’ method is usually preferred because it has no additional power losses [4,5]. Among the active damping methods, the capacitor current feedback control algorithm is important because it is simple to manipulate and is stable [6].

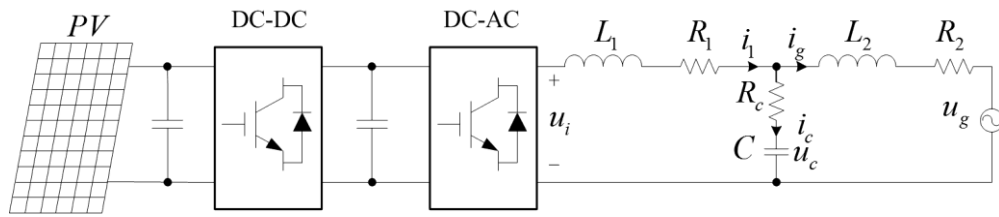
The quality of the injected grid current is important in grid-connected inverter control. Because of the infinite gain of the PR controller at the selected resonant frequency, the zero steady-state error can be achieved [7,8]. Papers in the literature do not discuss in detail the analysis of the frequency response influence between the PR controller and LCL filter. Moreover, the design methods of PR controllers and active damping of the LCL filter have not been well clarified. In most cases, many trial-and-error procedures have been carried out to obtain a set of parameters.

Considering the controller and the LCL filter active damping as a whole system enhances the complexity of controller design method. Their frequency responses may influence each other and affect the system stability. The design of the PI controller and the LCL filter active damping has been thoroughly investigated in [6]. However, a systematic study of the design procedures of the PR controller and the LCL filter active damping is missing. This paper discusses in detail such a design method. When adopting the PR controller instead of PI controller, the grid may produce a different impact on the inverter output current. The paper also deals with the grid impact and proposes a method to eliminate the grid effect on the output currents of the inverter.

2. System Overview and Numerical Modeling

Figure 1 shows the typical topology of a two-stage single-phase grid-connected photovoltaic (PV) system.

Figure 1. Two-stage single-phase grid-connected PV system with LCL filter typical topology.



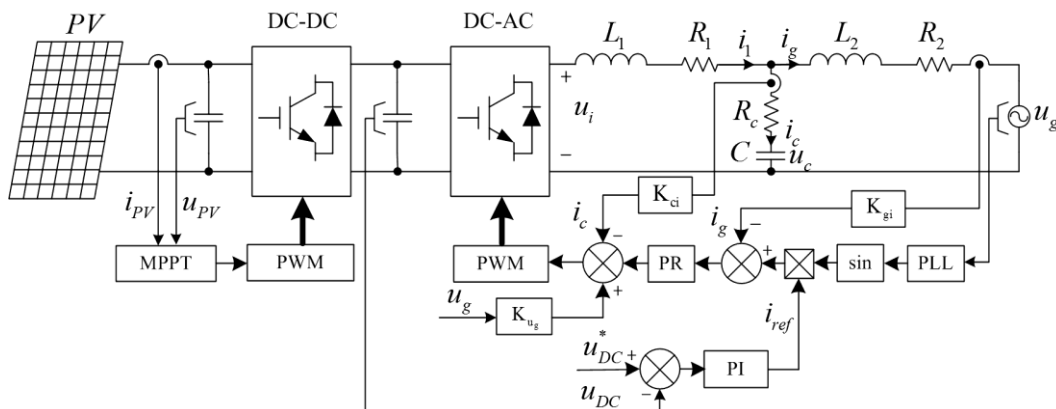
The series connected $L_1 + R_1$, $L_2 + R_2$ and $C + R_c$ that compose the LCL-type filter attenuate the harmonic injected into the grid generated from the inverter with the PWM technique. The boost DC-DC converter connected to the photovoltaic panel step up the voltage of the DC bus to a proper level for the DC-AC inverter. The H-bridge DC-AC inverter produces proper sinusoidal current in the grid with unity power factor based on the Maximum Power Point Tracking (MPPT) and Phase Locked Loop (PLL) algorithms. According to Figure 1, the mathematical model of the grid-connected inverter and the LCL filter is:

$$\begin{cases} L_1 \frac{di_1}{dt} + R_1 i_1 = u_i - u_c - R_c i_c \\ L_2 \frac{di_g}{dt} + R_2 i_g = u_c - u_g - R_c i_c \\ C \frac{du_c}{dt} = i_c \\ i_1 = i_g + i_c \end{cases} \quad (1)$$

3. Control Scheme

Figure 2 shows the PV system control scheme. By sampling the PV panel current and the voltage a proper MPPT algorithm can be ran. Papers in the literature present different MPPT algorithms [9–12]. The DC bus voltage control algorithm gives the injected current reference. Moreover, a PLL algorithm synchronizes the injected current with the grid voltage. Wide discussions on PLL algorithms for single-phase inverters can be found in various papers in the literature [13,14].

Figure 2. Two-stage single-phase PV system with LCL-filter control scheme.



The current reference is sinusoidal: since a PI controller is unable to track a sinusoidal reference without steady-state errors, the PR controller has been adopted. The PR controller tracks the current introducing an infinite gain at a certain frequency (resonant frequency) [8,15]. Sampling the LCL filter capacitor current modifies the control algorithm to perform an active damping; the active damping is mostly used to smooth the resonance peak of the LCL filter. The feedforward of grid voltage is essential and the following sections of the paper will focus on it.

According to Equation (1) and Figure 2, Figure 3 shows the control diagram of injected current. To simplify the analysis, resistors R_1 , R_2 , and R_c have been omitted: this corresponds to the worst LCL filter working condition. Figure 4 shows the equivalent control block diagram.

Figure 3. Injected current: control diagram.

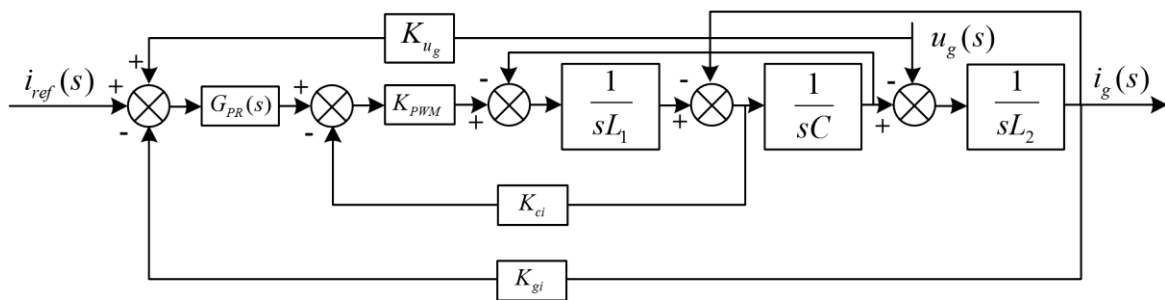
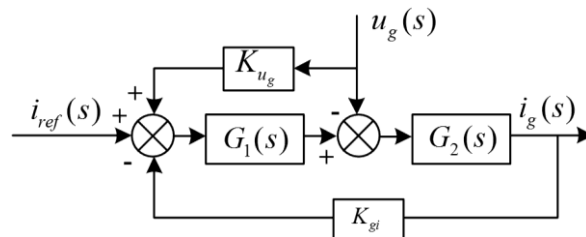


Figure 4. Equivalent control diagram.



where:

$$G_1(s) = \frac{G_{PR}(s)K_{PWM}}{s^2L_1C + sCK_{PWM}K_{ci} + 1} \tag{2}$$

$$G_2(s) = \frac{s^2L_1C + sCK_{PWM}K_{ci} + 1}{s^3L_1L_2C + s^2L_2CK_{PWM}K_{ci} + s(L_1 + L_2)} \tag{3}$$

3.1. PR Controller

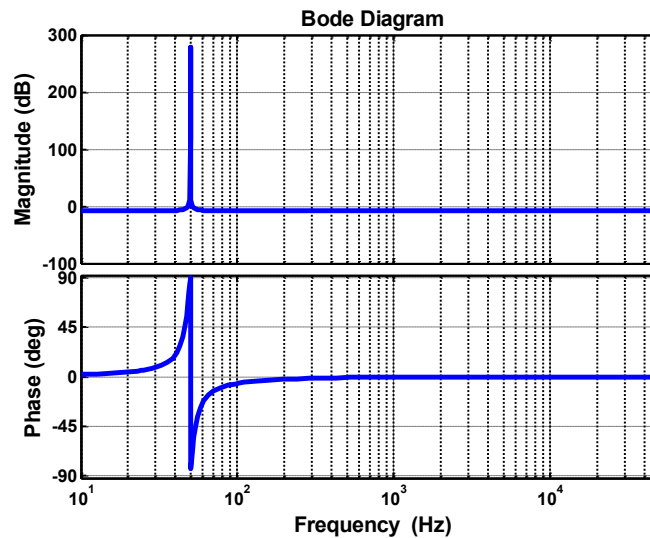
The Laplace transform of the ideal PR controller is:

$$G_{PR}(s) = K_p + \frac{2K_r s}{s^2 + \omega_1^2}$$

where K_p is the proportional gain and ω_1 , K_r are the resonant frequency and gain, respectively. The PI controller provides an infinite gain with a constant variable; it get a quick response to a step reference without steady-state error, but is unable to track a sinusoidal reference. On the contrary, the PR controller provides an infinite gain at the selected frequency (resonant frequency) and zero

phase-shift. Figure 5 shows the Bode diagram of an ideal PR controller. The controller cannot be realized in a physical circuit since it is lossless [8], and the improved form of the controller is a practical alternative.

Figure 5. Ideal PR controller Bode diagram.

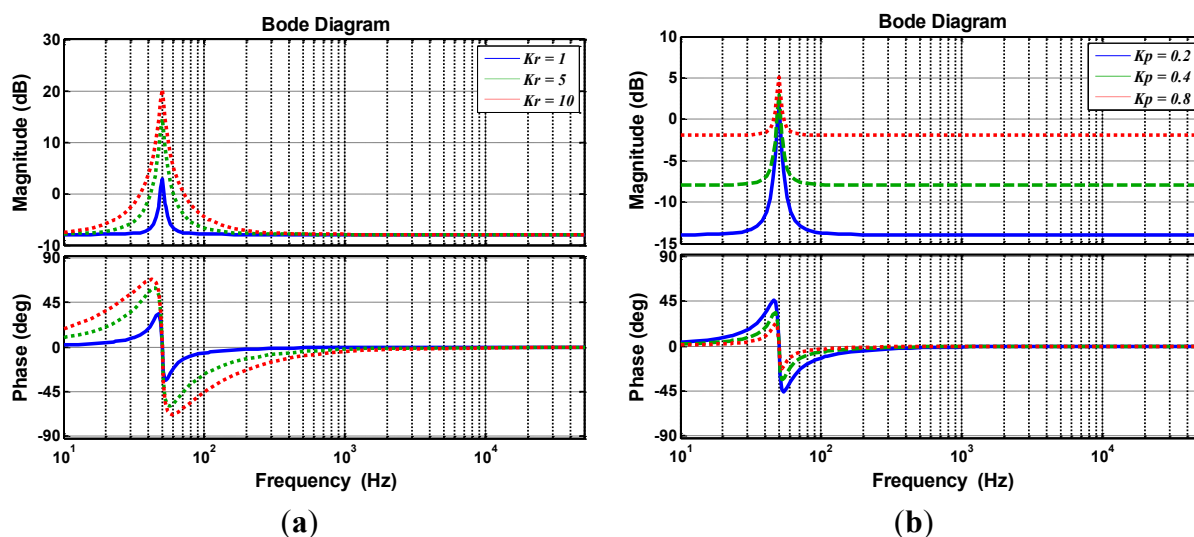


Equation (4) shows the PR controller improved form; the integral term has been approximated using a high-gain low-pass filter [8]:

$$G_{PR}(s) = K_p + \frac{2K_r \omega_{PRC} s}{s^2 + 2\omega_{PRC} s + \omega_1^2} \tag{4}$$

where ω_{PRC} is the bandwidth at -3 dB cutoff frequency of the controller that reduces the sensitivity of the grid fundamental frequency variation. The gain of the controller at $\omega_1 - \omega_{PRC}$ and $\omega_1 + \omega_{PRC}$ is $K_r / \sqrt{2}$ [8]. Figure 6 shows the Bode diagram of the improved PR controller. The proportional gain K_p mainly determines the dynamics of the controller, while K_r determines the amplitude gain at a selected frequency, and controls the bandwidth around it.

Figure 6. Improved PR controller Bode diagram: (a) $K_p = 0.4$; (b) $K_r = 1$.



3.2. LCL Filter

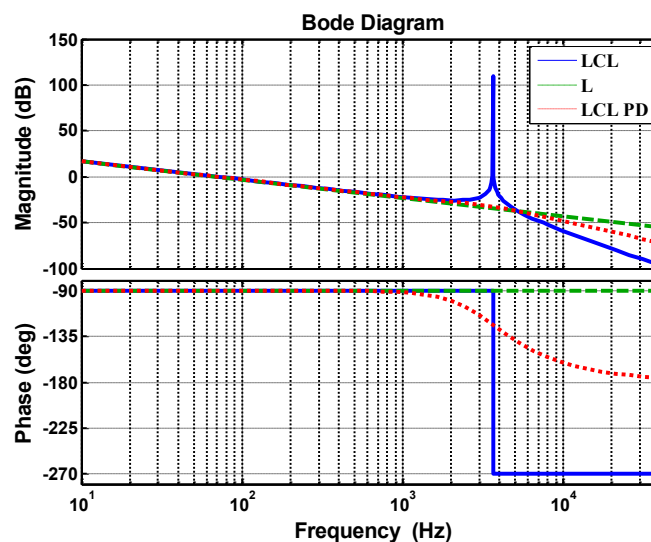
LCL filter is a high order system; the Laplace transfer function is given by following Equation (R_1 , R_2 , and R_c have been omitted):

$$G_{LCL}(s) = \frac{1}{s^3 L_1 L_2 C + s(L_1 + L_2)}$$

The LCL filter resonant frequency is:

$$f_{res} = \frac{1}{2\pi} \sqrt{\frac{L_1 + L_2}{L_1 L_2 C}}$$

Figure 7. LCL, and L filters Bode diagrams.



The LCL-filter provides outstanding performance attenuating the switching frequency current harmonics, better than the L- and LC-filters. Figure 7 compares the Bode diagram of the LCL and L filters. The red curve LCL PD (passive damping) represents the characteristic of the LCL-filter with a resistor connected in series with the capacitor. At low frequencies range, LCL and L filters show similar dynamic behaviors. At the high frequency range, LCL filter has stronger attenuation ability than the L-filter; this feature applies to medium and large power applications, since the very low switch frequency. As a drawbacks, the LCL filter presents resonance peaks around the resonant frequency and the phase-frequency curve across $-\pi$. As a result, systems become highly sensitive to disturbances and unstable, and the control algorithm design must consider the presence of an effective damping method.

The red curve LCL PD shows that the damping smooths the resonance peak, but worsens the LCL filter performance at the high frequency range, and generates additional power losses. Thus, an active damping method that modifies the control algorithm is preferable. This study adopts the active damping method based on the capacitor current feedback; the detailed design process is discussed later in the paper.

3.3. Grid Impact and Feedforward Control

With reference to Figure 4, the current injected into the grid can be written as:

$$i_g(s) = \frac{1}{K_{gi}} \frac{G(s)}{1+G(s)} i_{ref}(s) - \frac{1-K_{u_g}(s)G_1(s)}{1+G(s)} G_2(s)u_g(s) = i_{g1}(s) + i_{g2}(s) \quad (5)$$

where:

$$G(s) = G_1(s)G_2(s)K_{gi},$$

$$i_{g1}(s) = \frac{1}{K_{gi}} \frac{G(s)}{1+G(s)} i_{ref}(s), \text{ and}$$

$$i_{g2}(s) = -\frac{1-K_{u_g}(s)G_1(s)}{1+G(s)} G_2(s)u_g(s)$$

Defining the ratio between $i_{g2}(s)$ and $i_{g1}(s)$ as:

$$\sigma(s) = \frac{i_{g2}(s)}{i_{g1}(s)} = -\frac{[1-K_{u_g}(s)G_1(s)]G_2(s)u_g(s)K_{gi}}{G(s)i_{ref}(s)} \quad (6)$$

The grid can be treated as a disturb; omitting the feedforward from the grid the Equation (6) becomes:

$$\sigma(s) = \frac{i_{g2}(s)}{i_{g1}(s)} = -\frac{u_g(s)}{G_1(s)i_{ref}(s)} \quad (7)$$

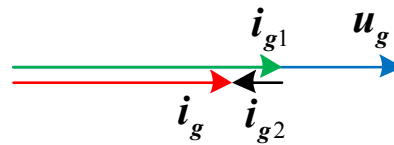
Taking the grid fundamental frequency as subject, the capacitor in LCL filter can be omitted since the resonant frequency of LCL filter is far greater than the fundamental frequency [6]. Thus, Equation (4) can be written as Equation (8):

$$G_{PR}(j\omega_1) = K_p + \frac{2K_r\omega_{PRc}j\omega_1}{(j\omega_1)^2 + 2\omega_{PRc}j\omega_1 + \omega_1^2} = K_p + K_r \quad (8)$$

Substituting Equations (7) and (8) into Equation (6), gives:

$$\sigma(j\omega_1) = -Z_g(j\omega_1) \frac{1}{K_{PWM}(K_p + K_r)} \quad (9)$$

where: $Z_g(j\omega_1) = \frac{u_g(s)}{i_{ref}(s)}$. $Z_g(j\omega_1)$ is the grid impedance at the fundamental frequency ω_1 . Because of the unity power factor, $Z_g(j\omega_1)$ is a pure resistor. Equation (9) shows the grid impact on the current: the grid-generated current i_{g2} flows in the opposite direction of the current i_{g1} . It is very different from a system that adopts PI controller as current controller [6] in which the grid generates a $\frac{\pi}{2}$ lag component to i_{g1} . According to Equations (5) and (9), the phase diagram of the grid can be drawn as Figure 8 shown:

Figure 8. Grid phase diagram.

Therefore, the feedforward of the grid is required; setting i_{g2} to zero, the feedforward factor becomes:

$$K_{u_g}(j\omega_1) = \frac{1}{G_1(j\omega_1)} = \frac{1}{K_{PWM}(K_p + K_r)} \quad (10)$$

If the feedforward control lies behind the PR controller, the feedforward factor has a very simple form:

$$K_{u_g}(j\omega_1) = \frac{1}{G_1(j\omega_1)} = \frac{1}{K_{PWM}} \quad (11)$$

4. PR Controller and Active-Damping of LCL Filter Design

4.1. PR Controller Design

4.1.1. Proportional Gain K_p

Assuming that the fundamental frequency of the grid varies in the range ± 1 Hz, ω_{PRc} is:

$$\omega_{PRc} = 2\pi \quad (12)$$

Following Equation describes the control diagram open-loop transfer function:

$$G(s) = G_1(s)G_2(s)K_{gi} \quad (13)$$

The relationship between the cutoff frequency f_c , the sampling frequency f_s , and the resonant frequency f_{res} is [6,16]:

$$f_c < \frac{1}{10} f_s, \text{ and } \frac{1}{4} f_s < f_{res} < \frac{1}{2} f_s$$

The cutoff frequency f_c of the system is usually designed to be far lower than the sampling frequency f_s , and much smaller than the resonant frequency f_{res} of LCL filter. Therefore, considering the frequency response of the system lower than the cutoff frequency, the capacitor of LCL filter can be omitted [6], and Equation (13) can be rewritten as Equation (14):

$$G(s) \approx \frac{K_{gi} K_{PWM} G_{PR}(s)}{s(L_1 + L_2)} \quad (14)$$

The cutoff frequency f_c is higher than the fundamental frequency f_1 . As a result, according to Figure 6 the PR controller expression simplifies. At cutoff frequency, the magnitude frequency response of the system is zero, and Equation (15) is obtained:

$$20 \lg |G(j2\pi f_c)| \approx 20 \lg \left| \frac{K_{gi} K_{PWM} K_p}{j2\pi f_c (L_1 + L_2)} \right| = 0 \tag{15}$$

By successive approximations of Equation (15), the gain K_p is:

$$K_p \approx \frac{2\pi f_c (L_1 + L_2)}{K_{gi} K_{PWM}} \tag{16}$$

4.1.2. Fundamental Frequency Gain K_r

The tracking steady-state error of the grid current i_g can be calculated as:

$$E_g(s) = \frac{K_{gi} [i_{g1}(s) + i_{g2}(s)] - i_{ref}(s)}{i_{ref}(s)} = \frac{G(s)}{1 + G(s)} - \frac{[1 - K_{u_g}(s)G_1(s)]K_{gi}G_2(s)Z_g(s)}{1 + G(s)} - 1 \tag{17}$$

Assuming the adoption of grid feedforward control, Equation (17) can be simplified as:

$$E_g(s) = \frac{K_{gi} i_{g1}(s) - i_{ref}(s)}{i_{ref}(s)} = \frac{G(s)}{1 + G(s)} - 1 \tag{18}$$

Considering the fundamental frequency f_1 , and supposing the steady-state error of i_g is η , following Equation gives the minimum of the magnitude-frequency response of open-loop transfer function at the fundamental frequency f_1 :

$$|G_{\min}(j2\pi f_1)| = \frac{1}{\eta} - 1$$

That is:

$$|G(j2\pi f_1)| \approx \left| \frac{K_{gi} K_{PWM} G_{PR}(j2\pi f_1)}{j2\pi f_1 (L_1 + L_2)} \right| \geq |G_{\min}(j2\pi f_1)| \tag{19}$$

Taking Equation (16) into Equation (19), the lower threshold of K_r is deduced as:

$$K_r \geq \frac{(2\pi f_1 |G_{\min}(j2\pi f_1)| - 2\pi f_c)(L_1 + L_2)}{K_{gi} K_{PWM}} \tag{20}$$

The phase-frequency response of PR controller can be written as:

$$\varphi(\omega) = \arctan \frac{2\omega_{PRc}\omega}{\omega_1^2 - \omega^2} \left(1 + \frac{K_r}{K_p}\right) - \arctan \frac{2\omega_{PRc}\omega}{\omega_1^2 - \omega^2} \tag{21}$$

As the improved PR controller Bode plot shows (Figure 6), the larger K , the larger gain at the fundamental frequency is. It is beneficial to the quick response speed, but it emphasizes an extra drawback. The phase response of the controller tends to $-\frac{\pi}{2}$ as K_r increases, which would affect the phase margins of the whole PV system. Therefore, a compromise between the response speed and the stability is required. Assuming the phase-frequency response of PR controller at cutoff frequency not exceeds $-\phi$, and that the phase response of the other components at cutoff frequency must not exceed $(PM - \pi + \phi)$, following Equation (22) describes the phase:

$$\varphi(\omega_c) = \arctan \frac{2\omega_{PRc}\omega_c}{\omega_1^2 - \omega_c^2} \left(1 + \frac{K_r}{K_p}\right) - \arctan \frac{2\omega_{PRc}\omega_c}{\omega_1^2 - \omega_c^2} \geq -\phi \quad (22)$$

Taking Equation (16) into Equation (22), the upper threshold of K_r is:

$$K_r \leq \frac{\omega_c(L_1 + L_2)}{K_{gi}K_{PWM}} \left[\frac{\omega_1^2 - \omega_c^2}{2\omega_{PRc}\omega_c} \tan(\arctan \frac{2\omega_{PRc}\omega_c}{\omega_1^2 - \omega_c^2} - \phi) - 1 \right] \quad (23)$$

According to Equations (20) and (23), the range of K_r is defined through Equation (24):

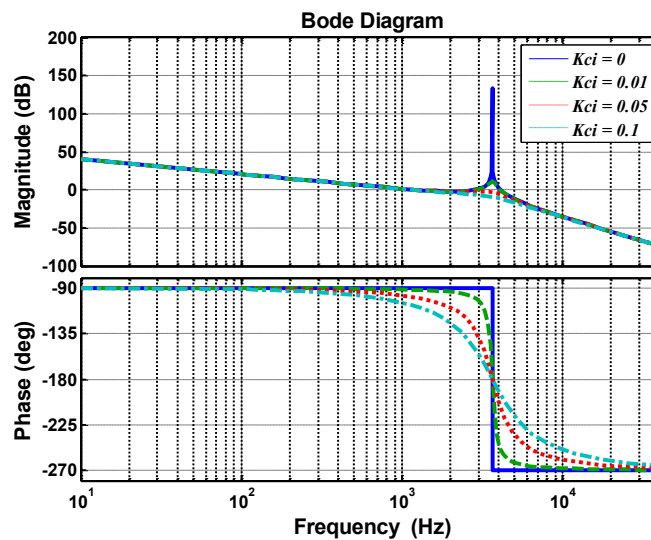
$$\frac{(\omega_1 |G_{\min}(j\omega_1)| - \omega_c)(L_1 + L_2)}{K_{gi}K_{PWM}} \leq K_r \leq \frac{\omega_c(L_1 + L_2)}{K_{gi}K_{PWM}} \left[\frac{\omega_1^2 - \omega_c^2}{2\omega_{PRc}\omega_c} \tan(\arctan \frac{2\omega_{PRc}\omega_c}{\omega_1^2 - \omega_c^2} - \phi) - 1 \right] \quad (24)$$

4.2. Active-Damping of LCL Filter

Figure 9 shows the Bode diagram of the PV system with no PR controller. A high value of K_{ci} shows better resonance peak damping capability, but phase margins become smaller. The reciprocal of magnitude-response at the LCL filter resonant frequency corresponds to the grid-connected system magnitude margins (GM). Thus, Equation (25) can be written as:

$$-20\lg|G(j2\pi f_r)| = -20\lg \left| \frac{K_{gi}K_{PWM}G_{PR}(j2\pi f_r)}{(j2\pi f_r)^3 L_1 L_2 C + (j2\pi f_r)^2 L_2 C K_{ci} K_{PWM} + j2\pi f_r(L_1 + L_2)} \right| \geq GM \quad (25)$$

Figure 9. System with no PR controller: Bode diagram.



Since the resonant frequency is far from the fundamental frequency, the PR controller can be considered as a proportional component. Taking Equation (16) into Equation (25), the lower threshold of K_{ci} is:

$$K_{ci} \geq \frac{2\pi f_c L_1}{K_{PWM}} 10^{\frac{GM}{20}} \quad (26)$$

The phase margins (PM) of the whole system can be written as:

$$\pi + \varphi(G(j2\pi f_c)) \geq PM$$

Thus:

$$\frac{\pi}{2} + \arctan\left[\left(\frac{K_r}{K_p} + 1\right) \frac{2\omega_{PRC}\omega_c}{\omega_1^2 - \omega_c^2}\right] - \arctan\left(\frac{2\omega_{PRC}\omega_c}{\omega_1^2 - \omega_c^2}\right) - \arctan\left[\frac{K_{ci}K_{PWM}\omega_c}{L_1(\omega_r^2 - \omega_c^2)}\right] \geq PM \tag{27}$$

The superior threshold of K_{ci} can be written as Equation (28):

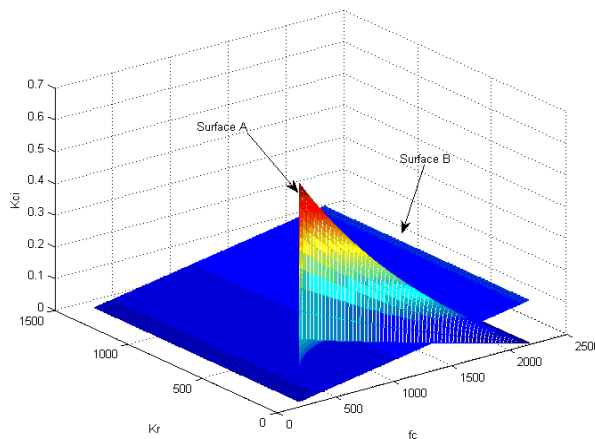
$$K_{ci} \leq \frac{L_1(\omega_r^2 - \omega_c^2) \tan\left(\frac{\pi}{2} + \arctan\left[\left(\frac{K_r}{K_p} + 1\right) \frac{2\omega_{PRC}\omega_c}{\omega_1^2 - \omega_c^2}\right] - \arctan\left(\frac{2\omega_{PRC}\omega_c}{\omega_1^2 - \omega_c^2}\right) - PM\right)}{K_{PWM}\omega_c} \tag{28}$$

According to Equations (26) and (28) the range of the K_{ci} is given by Equation (29):

$$\frac{\omega_c L_1}{K_{PWM}} 10^{\frac{GM}{20}} \leq K_{ci} \leq \frac{L_1(\omega_r^2 - \omega_c^2) \tan\left(\frac{\pi}{2} + \arctan\left[\left(\frac{K_r}{K_p} + 1\right) \frac{2\omega_{PRC}\omega_c}{\omega_1^2 - \omega_c^2}\right] - \arctan\left(\frac{2\omega_{PRC}\omega_c}{\omega_1^2 - \omega_c^2}\right) - PM\right)}{K_{PWM}\omega_c} \tag{29}$$

According to Equations (24) and (29) the relationship between f_c , K_r and K_{ci} can be represented in a 3-D plot. Figure 10 shows the relationship between the three above-mentioned parameters; the space surrounded by Surface A and Surface B indicates the satisfactory range of the K_r and K_{ci} at a specific f_c :

Figure 10. Relationship between f_c , K_r and K_{ci} .



5. Numerical Simulation and Experimental Results

Following Table 1 summarizes simulation and experimental parameters.

Table 1. System parameters.

Name	Value
Fundamental frequency f_1	50 Hz
Switching frequency f_s	12 kHz
Grid phase voltage (RMS)	220 V
Grid current factor feedback K_{gi}	0.04
LCL filter inductor L_1	1.88 mH
LCL filter inductor L_2	0.34 mH
LCL filter capacitor C	6.6 μ F

This section describes a practical example using parameters of Table 1. According to parameters, the calculated resonant frequency of LCL filter is 3.65 kHz. The cutoff frequency is defined as $f_c < \frac{f_s}{10}$, and the selected value of f_c is 900 Hz.

(1) The calculated proportional gain K_p (Equation (16)) is:

$$K_p \approx \frac{2\pi f_c (L_1 + L_2)}{K_{gi} K_{PWM}} = 0.83$$

(2) The resonant factor K_r range has been calculated (Equation (24)):

Supposing the steady-state tracking error of i_g is 1%, the minimum of the magnitude-frequency response of open-loop transfer function at the fundamental frequency f_1 equals 99. Assuming the minimum phase-frequency response of PR controller at the cutting frequency $-\phi$ is -10° . Therefore, resonance factor K_r range is:

$$K_{r\min} < K_r < K_{r\max}$$

where $K_{r\min} = 3.717$, and $K_{r\max} = 41.075$.

(3) The active-damping factor K_{ci} range has been calculated through Equation (29):

Supposing the magnitude margin of the system equals 3 dB, and the phase margin 45° , thus:

$$K_{ci\min} < K_{ci} < K_{ci\max}$$

where $K_{ci\min} = 0.039$, $K_{ci\max} = 0.364$.

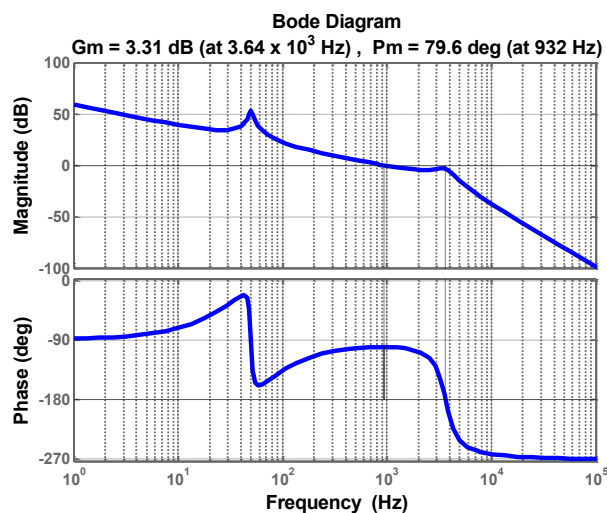
Considering the previous three steps, a set of proper parameters can be defined:

$$K_p = 0.8, K_r = 20, K_{ci} = 0.04$$

Moreover, the calculated feedforward factor of the grid voltage K_{u_g} equals 0.44.

MATLAB/Simulink toolbox helps verifying the feasibility of design parameters method. Figure 11 shows the system Bode diagram, based on the above-mentioned parameters. The magnitude margin (3.31 dB) and the phase margin (79.6 degrees), both confirm the stability of the system.

Figure 11. System Bode diagram.



However, it is impossible to manufacture a filter whose parameters completely match the initial design. Moreover, parameters change while filter operates; the grid impedance must be considered, since inductive impedance of long cables and low power transformers. Therefore, the current controller parameters must be enough robust against the parameters variation. Since the inductor L_2 is connected in series to the grid, the grid impedance variation can be merged with L_2 variation. Figures 12–14 depict the Bode plots of the system. Current controller has been designed using the aforementioned method under different parameter variations.

Figure 12. System Bode diagram under different parameters: (a) inductor L_1 increased by 20%; (b) inductor L_1 decreased by 20%.

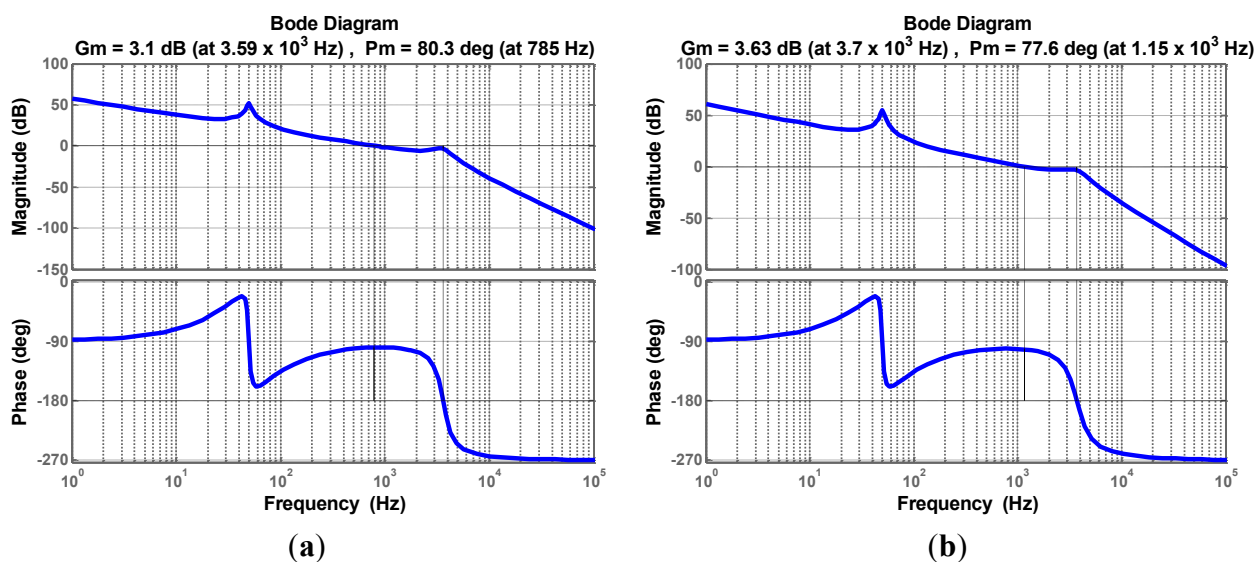


Figure 13. System Bode diagram under different parameters: (a) capacitor C increased by 20%; (b) capacitor C decreased by 20%.

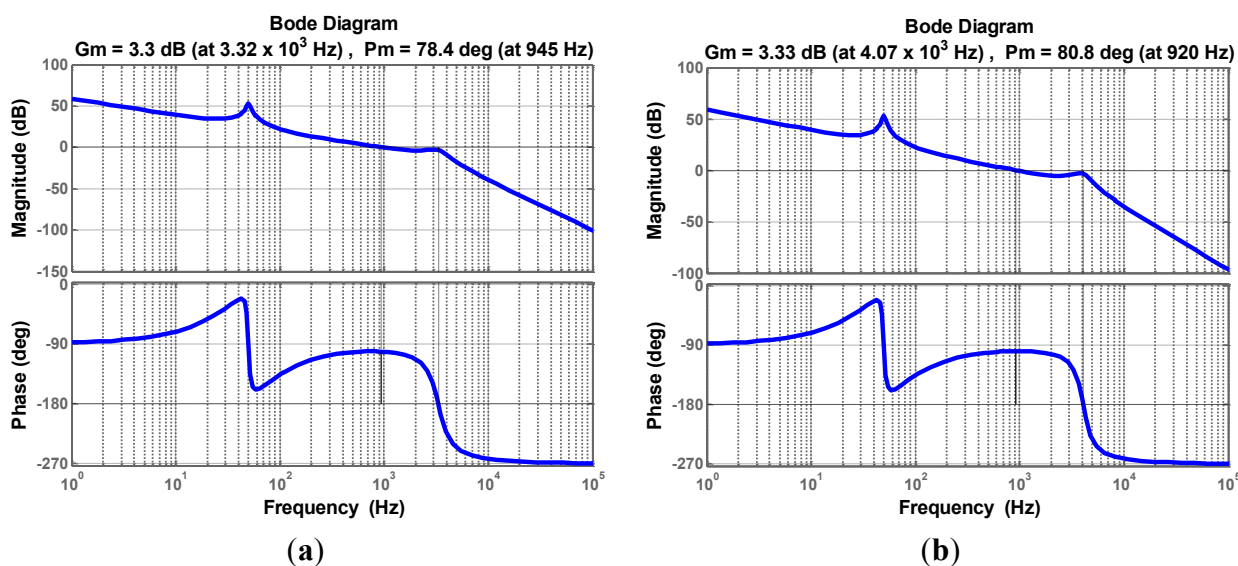


Figure 14. System Bode diagram under different parameters: (a) inductor L_2 increased by 150%; (b) inductor L_2 decreased by 20%.

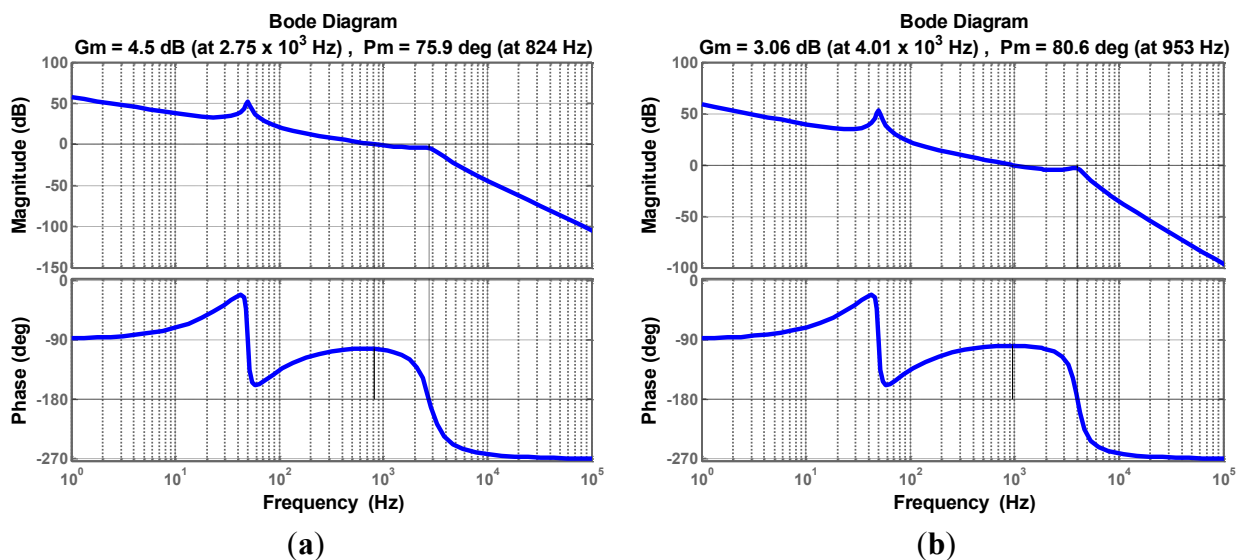


Table 2 summarizes the results shown in previous Figures 12–14. Since the controller design considered well the system stability margin requirements, the system is stable even with important changes in parameters, in the range -20% to 20% (in case of inductor L_2 the range extends from -20% to 250%). The minimum system magnitude margin is higher than 3 dB and the minimum phase margin is higher than 75 degrees. Therefore, the current controller parameters obtained by applying the proposed method enhance robustness against system parameters variation.

Table 2. System Magnitude and Phase margins with different parameters.

Stable margins	Nominal parameters	L_1		C		L_2	
		Increased by 20%	Decreased by 20%	Increased by 20%	Decreased by 20%	Increased by 150%	Decreased by 20%
Magnitude margin	3.31 dB	3.1 dB	3.63 dB	3.3 dB	3.33 dB	4.5 dB	3.06 dB
Phase margin	79.6 degree	80.3 degree	77.6 degree	78.4 degree	80.8 degree	75.9 degree	80.6 degree

5.1. Numerical Simulation Results

Besides the filter parameters and grid impedance variation, the grid voltage is not always stable. Therefore, we must test the robustness of the grid-connected system against grid voltage fluctuations. The application of the proposed method gives the current controller parameters. Figures 15–18 below show the simulation results of grid voltage fluctuation and injected current at full load under different parameter variation conditions. All simulations give the grid voltage sag equals about 42 V and voltage swell equals about 30 V. Figure 15 shows that with the nominal LCL-filter the injected current remains stable during the grid voltage sag or voltage swell. The grid fluctuation does not affect the system stability. According to the Bode diagrams shown in Figures 12–14 the stable margins of the system are enough even with important changes in parameters. Figures 16–18 show that the injected current is stable under nominal grid voltage with filter parameters variation. Moreover, even when the grid fluctuates, the system remains stable, as a confirmation of the effectiveness of the controller against

filter parameters variation and grid fluctuations. If the inverter is connected to a weak grid (a very common situation in rural areas), the grid impedance is inductive and it can be regarded as equivalent to the increasing of inductor L_2 . In this study, L_2 increases by 150% its value to simulate a weak grid situation. Even if the grid is weak and fluctuates, the overall system remains stable as Figure 17a,b shows.

Figure 15. Grid voltage and injected current at full load with nominal parameters: simulation results. (a) Grid voltage sag; (b) grid voltage swell.

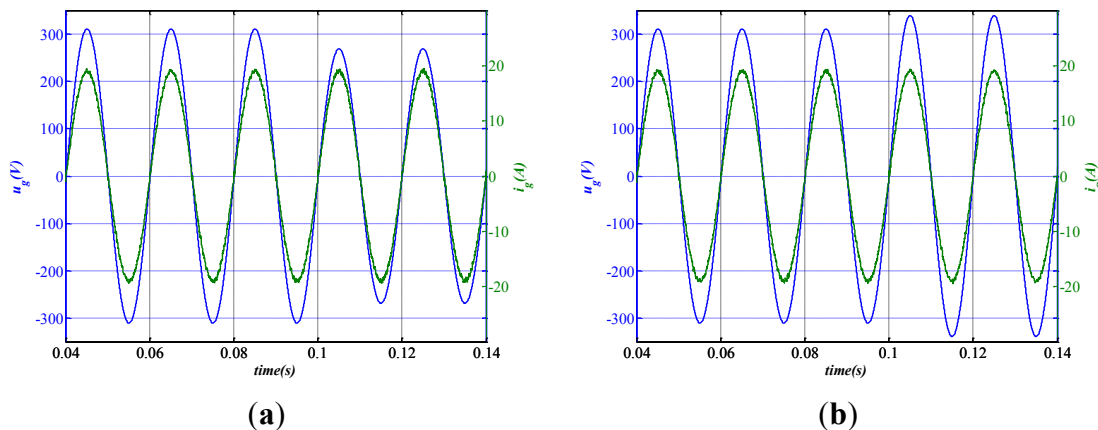


Figure 16. Grid voltage and injected current at full load with inductor L_1 variation: simulation results. (a) Inductor L_1 increased by 20%: grid voltage sag; (b) Inductor L_1 increased by 20%: grid voltage swell; (c) Inductor L_1 decreased by 20%: grid voltage sag; (d) Inductor L_1 decreased by 20%: grid voltage swell.

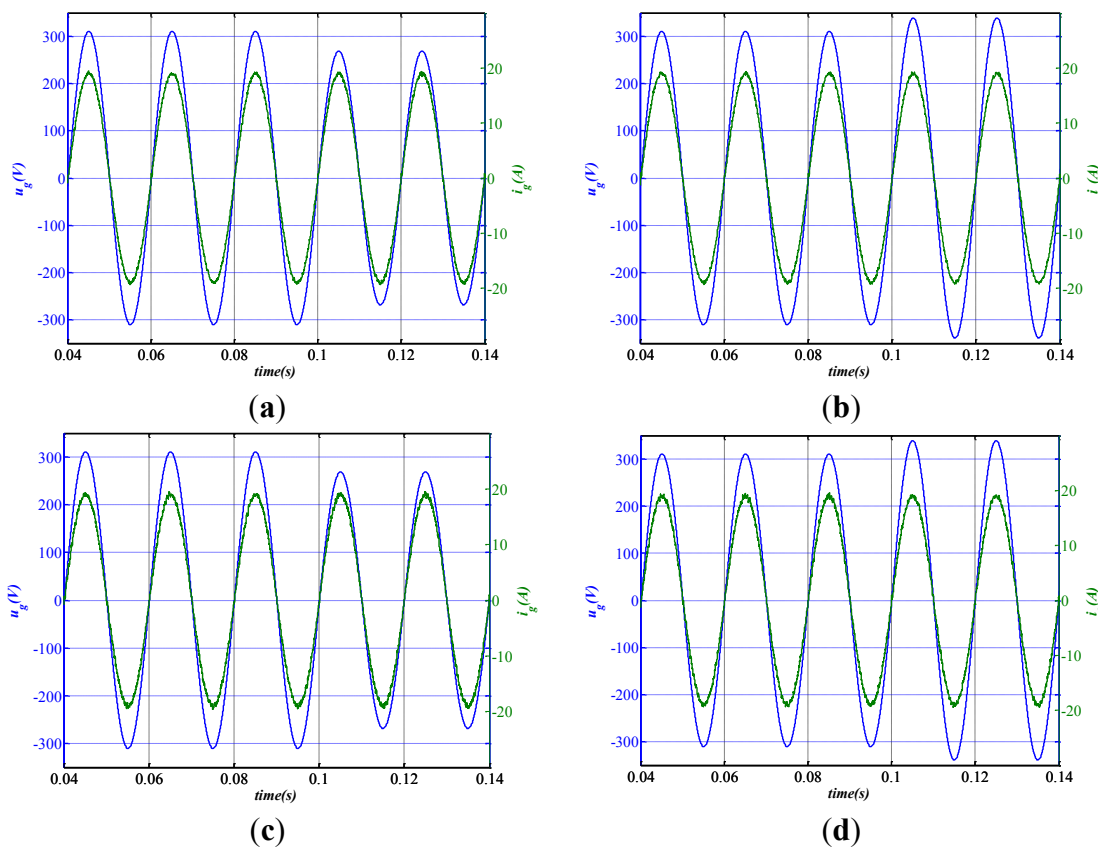


Figure 17. Grid voltage and injected current at full load with inductor L_2 variation: simulation results. (a) Inductor L_2 increased by 150%: grid voltage sag; (b) inductor L_2 increased by 150%: grid voltage swell; (c) inductor L_2 decreased by 20%: grid voltage sag; (b) inductor L_2 decreased by 20%: grid voltage swell.

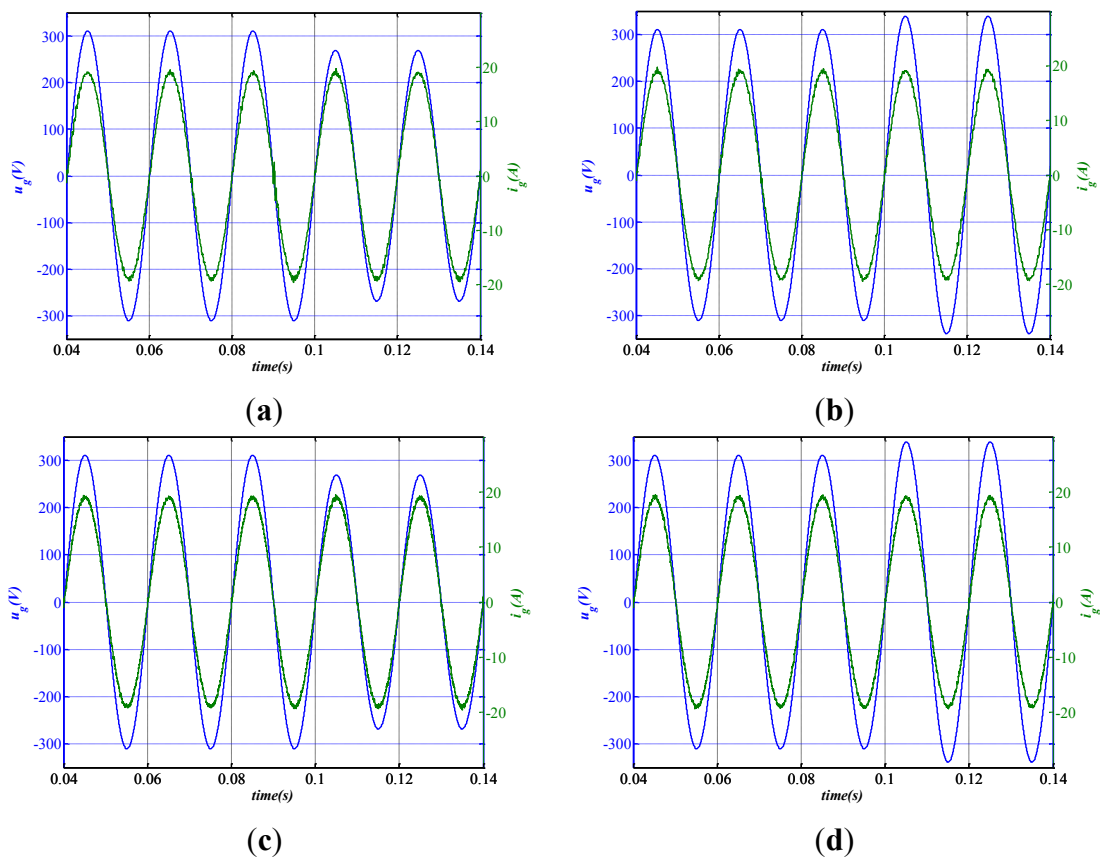


Figure 18. Grid voltage and injected current at full load with capacitor C variation: simulation results. (a) Capacitor C increased by 20%: grid voltage sag; (b) capacitor C increased by 20%: grid voltage swell; (c) capacitor C decreased by 20%: grid voltage sag; (b) capacitor C decreased by 20%: grid voltage swell.

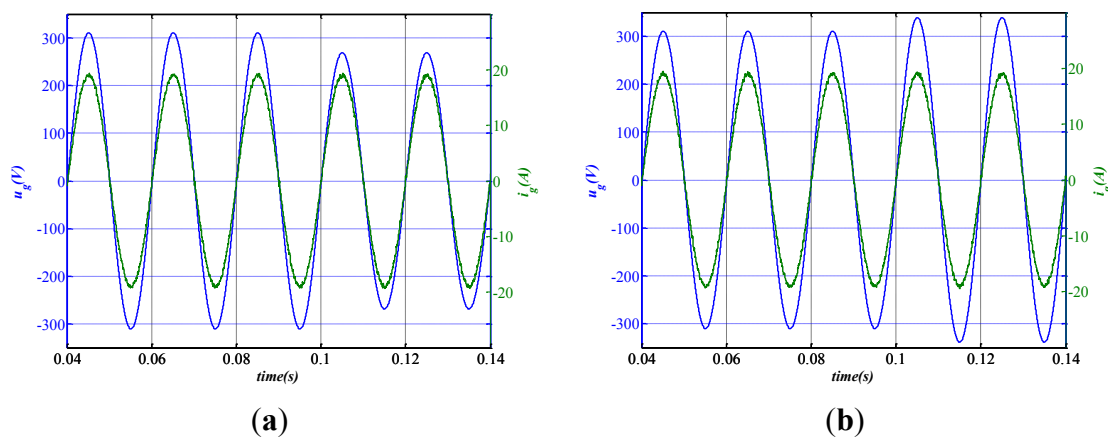
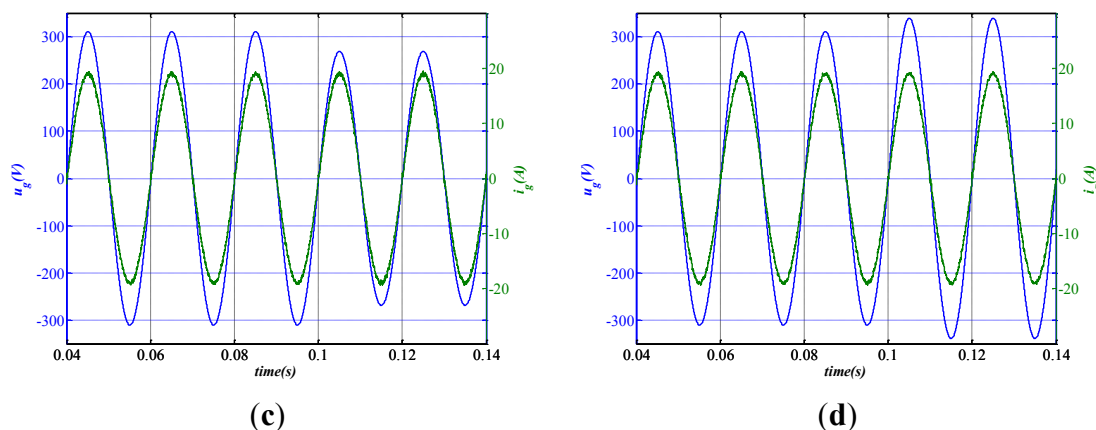


Figure 18. Cont.



5.2. Experimental Results

The design parameters have been verified through a 3-kW experimental setup. Inductors, capacitors, and other parameters have been set as in the corresponding simulations described in previous sections. All of the PV system algorithms have been implemented on a digital signal processor TMS320F2808 (Texas Instruments, Dallas, TX, USA). The PR controller has been discretized using the Tustin method with frequency pre-warping [17] for poles and zeroes, that yields a better matching frequency response. The adoption of the unipolar modulation SPWM regulated the injected grid current and a PV simulator replaced the PV panel. The DC source of DC-AC inverter has been given through the Boost DC-DC converter by applying the P&O MPPT method that guarantees simplicity and effectiveness [9–12]. To simulate the grid voltage fluctuation, a Programmable AC Power Source replaced the grid, while the voltage sag and swell values have been set equals to numerical simulation. Figures 19–22 show the experimental waveforms at full load under different parameters variations; the simulation results and the experimental data have been plot into one-to-one correspondence. Although the experimental results are worse than the numerical simulation ones because of the parasitic parameters of the inductors and capacitor, they are still very satisfactory. The experimental data well match numerical simulations.

Figure 19. Grid voltage and injected current at full load with nominal parameters: experimental results. (a) Grid voltage sag; (b) grid voltage swell.

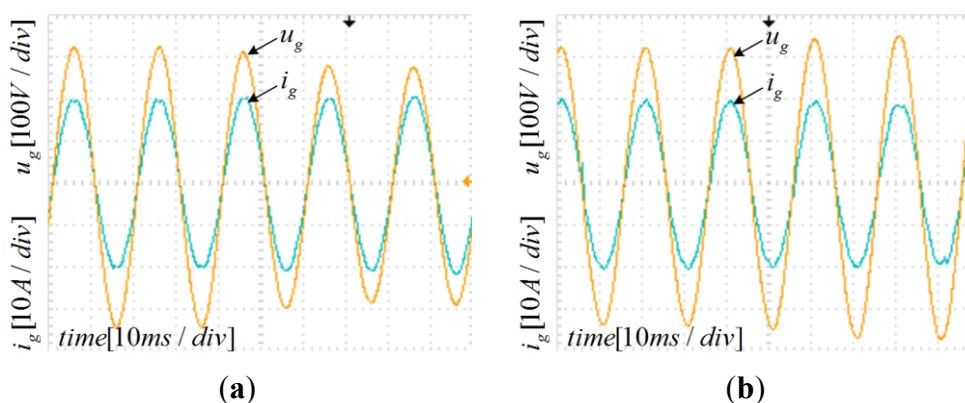


Figure 20. Grid voltage and injected current at full load with inductor L_1 variation: experimental results. (a) Inductor L_1 increased by 20%: grid voltage sag; (b) inductor L_1 increased by 20%: grid voltage swell; (c) inductor L_1 decreased by 20%: grid voltage sag; (b) inductor L_1 decreased by 20%: grid voltage swell.

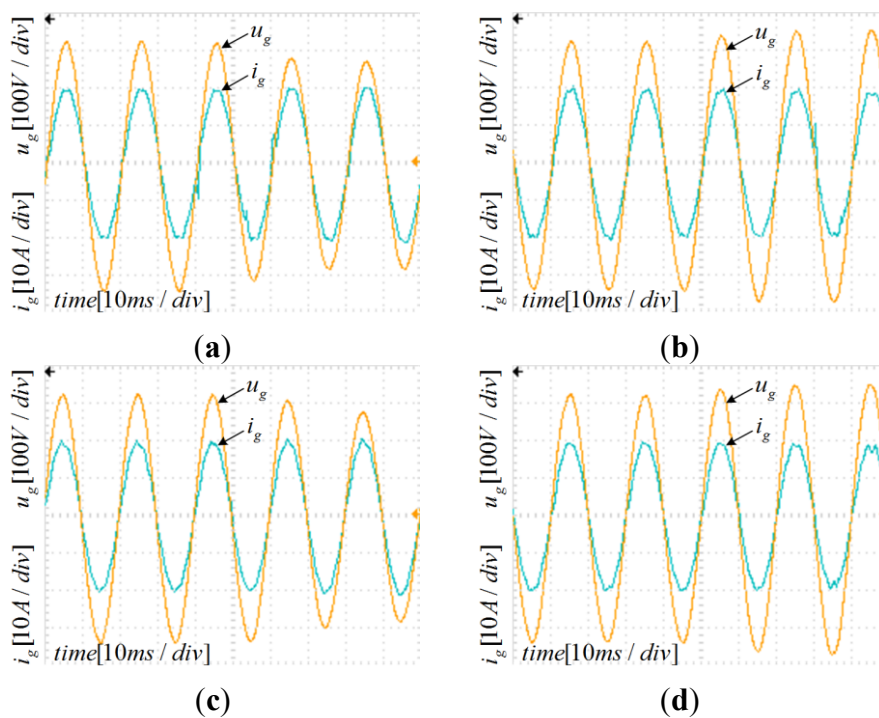


Figure 21. Grid voltage and injected current at full load with inductor L_2 variation: experimental results. (a) Inductor L_2 increased by 150%: grid voltage sag; (b) inductor L_2 increased by 150%: grid voltage swell; (c) inductor L_2 decreased by 20%: grid voltage sag; (b) inductor L_2 decreased by 20%: grid voltage swell.

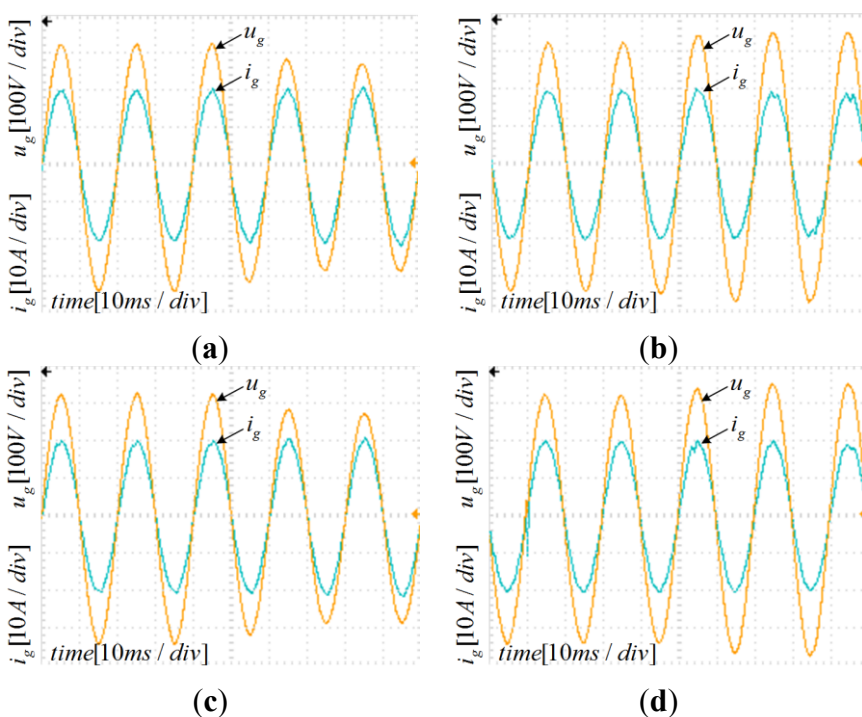
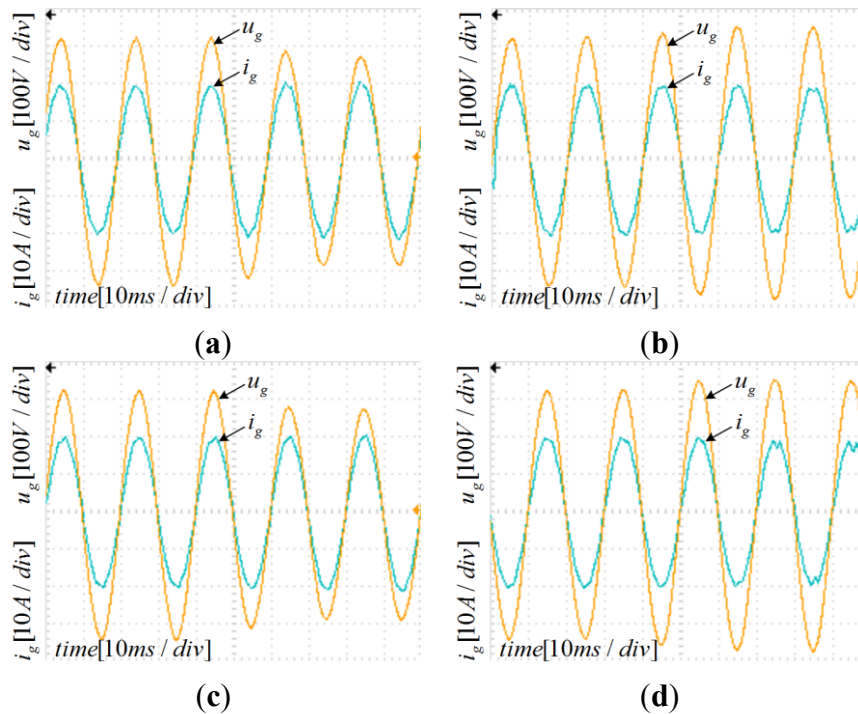


Figure 22. Grid voltage and injected current at full load with capacitor C variation: experimental results. **(a)** Capacitor C increased by 20%: grid voltage sag; **(b)** capacitor C increased by 20%: grid voltage swell; **(c)** capacitor C decreased by 20%: grid voltage sag; **(d)** capacitor C decreased by 20%: grid voltage swell.



6. Conclusions

The stability analysis of the system composed by a PR controller and an LCL filter together is not easy: the frequency responses may affect each other and the PR controller design becomes complex. The traditional method based on trial-and-error procedures, is too time-consuming, and the design process is inefficient. This paper provides a detailed analysis of the frequency response influence between the PR controller and the LCL filter. In addition, the paper presents a systematic design method for the PR controller parameters and the capacitor current feedback coefficient, used in the active damping of the LCL filter. Using the new parameters, a numerical simulation shows that the system meets the requirements of stable margins and current tracking steady-state error. The robustness of the current controller is verified through several experimental tests carried out on a 3 kW platform varying the system parameters. The Bode diagrams of the system varying inductor, capacitor, and grid impedance values confirmed that the controller parameters enhance robustness against the system parameters variation. Moreover, the system remains stable even in case of grid voltage fluctuation. Both the simulation and the experimental results assess the validity of the proposed design method.

Author Contributions

Ningyun Zhang developed the idea of the paper, and Chen Yao contributed to the discussion of the results. Ningyun Zhang performed the experiments and wrote the paper. Houjun Tang gave some suggestions to the paper writing. All authors have given approval to the final version of the manuscript.

Conflicts of Interest

The authors declare no conflict of interest.

References

1. Carrasco, J.M.; Franquelo, L.G.; Bialasiewicz, J.T.; Galvan, E.; Guisado, R.C.P.; Prats, A.M.; Leon, J.I.; Moreno-Alfonso, N. Power-electronic systems for the grid integration of renewable energy sources: A survey. *IEEE Trans. Ind. Electron.* **2006**, *53*, 1002–1016.
2. Wessels, C.; Dannehl, J.; Fuchs, F.W. Active Damping of LCL-Filter Resonance based on Virtual Resistor for PWM Rectifiers—Stability Analysis with Different Filter Parameters. In Proceedings of the 2008 IEEE Power Electronics Specialists Conference, Rhodes, Greece, 15–19 June 2008; pp. 3532–3538.
3. Castilla, M.; Miret, J.; Matas, J.; de Vicuna, L.G.; Guerrero, J.M. Control design guidelines for single-phase grid-connected photovoltaic inverters with damped resonant harmonic compensators. *IEEE Trans. Ind. Electron.* **2009**, *56*, 4492–4501.
4. Yi, L.; Zhengming, Z.; Fanbo, H.; Sizhao, L.; Lu, Y. An Improved Virtual Resistance Damping Method for Grid-Connected Inverters with LCL Filters. In Proceedings of the 2011 IEEE Energy Conversion Congress and Exposition (ECCE 2011), Phoenix, AZ, USA, 17–22 September 2011; pp. 3816–3822.
5. Parker, S.G.; McGrath, B.P.; Holmes, D.G. Regions of Active Damping Control for LCL Filters. In Proceedings of the Energy Conversion Congress and Exposition (ECCE), Raleigh, NC, USA, 15–20 September 2012; pp. 53–60.
6. Bao, C.L.; Ruan, X.B.; Wang, X.H.; Li, W.W.; Pan, D.H.; Weng, K.L. Design of Injected Grid Current Regulator and Capacitor-Current-Feedback Active-Damping for LCL-Type Grid-Connected Inverter. In Proceedings of the Energy Conversion Congress and Exposition (ECCE), Raleigh, NC, USA, 15–20 September 2012; pp. 579–586.
7. Fukuda, S.; Yoda, T. A novel current-tracking method for active filters based on a sinusoidal internal model. *IEEE Trans. Ind. Appl.* **2001**, *37*, 888–895.
8. Zmood, D.N.; Holmes, D.G. Stationary frame current regulation of PWM inverters with zero steady-state error. *IEEE Trans. Power Electron.* **2003**, *18*, 814–822.
9. Eram, T.; Chapman, P.L. Comparison of photovoltaic array maximum power point tracking techniques. *IEEE Trans. Energy Convers.* **2007**, *22*, 439–449.
10. Noguchi, T.; Togashi, S.; Nakamoto, R. Short-current pulse-based maximum-power-point tracking method for multiple photovoltaic-and-converter module system. *IEEE Trans. Ind. Electron.* **2002**, *49*, 217–223.
11. Mutoh, N.; Ohno, M.; Inoue, T. A method for MPPT control while searching for parameters corresponding to weather conditions for PV generation systems. *IEEE Trans. Ind. Electron.* **2006**, *53*, 1055–1065.
12. Petrone, G.; Spagnuolo, G.; Vitelli, M. A multivariable perturb-and-observe maximum power point tracking technique applied to a single-stage photovoltaic inverter. *IEEE Trans. Ind. Electron.* **2011**, *58*, 76–84.

13. Ciobotaru, M.; Teodorescu, R.; Blaabjerg, F. A New Single-Phase PLL Structure Based on Second Order Generalized Integrator. In Proceedings of the 2006 IEEE Power Electronics Specialists Conference (IEEE Cat. No. 06CH37819C), Jeju, Korea, 18–22 June 2006; pp. 1–6.
14. Silva, S.M.; Lopes, B.M.; Cardoso, B.J.; Campana, R.P.; Boaventura, W.C. Performance Evaluation of PLL Algorithms for Single-Phase Grid-Connected Systems. In Conference Record of the 2004 IEEE Industry Applications Conference, Seattle, WA, USA, 3–7 October 2004; Volumes 1–4, Covering Theory to Practice, pp. 2259–2263.
15. Zmood, D.N.; Holmes, D.G.; Bode, G.H. Frequency-domain analysis of three-phase linear current regulators. *IEEE Trans. Ind. Appl.* **2001**, *37*, 601–610.
16. Dannehl, J.; Wessels, C.; Fuchs, F.W. Limitations of voltage-oriented PI current control of grid-connected pwm rectifiers with LCL filters. *IEEE Trans. Ind. Electron.* **2009**, *56*, 380–388.
17. Yepes, A.G.; Freijedo, F.D.; Doval-Gandoy, J.; Lopez, O.; Malvar, J.; Fernandez-Comesana, P. Effects of discretization methods on the performance of resonant controllers. *IEEE Trans. Power Electron.* **2012**, *27*, 4976.

© 2014 by the authors; licensee MDPI, Basel, Switzerland. This article is an open access article distributed under the terms and conditions of the Creative Commons Attribution license (<http://creativecommons.org/licenses/by/3.0/>).